Editors' Suggestion

Radial and orbital decomposition of charge radii of Ca nuclei: Comparative study of Skyrme and Fayans functionals

T. Inakura [1,2,*] N. Hinohara [3,4,5,†] and H. Nakada [6,7,‡]

[1]*Office of Institutional Research and Decision Support, Tokyo Institute of Technology, Meguro, Tokyo 152-8550, Japan*
[2]*Laboratory for Zero-Carbon Energy, Institute of Innovative Research, Tokyo Institute of Technology, Meguro, Tokyo 152-8550, Japan*
[3]*Center for Computational Sciences, University of Tsukuba, Tsukuba, Ibaraki 305-8577, Japan*
[4]*Faculty of Pure and Applied Sciences, University of Tsukuba, Tsukuba, Ibaraki 305-8571, Japan*
[5]*Facility for Rare Isotope Beams, Michigan State University, East Lansing, Michigan 48824, USA*
[6]*Department of Physics, Graduate School of Science, Chiba University, Yayoi-cho 1-33, Inage, Chiba 263-8522, Japan*
[7]*Research Center for Nuclear Physics, Osaka University, Mihogaoka 10-1, Ibaraki, Osaka 567-0047, Japan*

(Received 20 April 2024; accepted 23 September 2024; published 14 November 2024)

We investigate the charge and point-proton radii of Ca nuclei in detail using a density functional theory framework. The Fayans energy density functional (EDF) provides a characteristic N dependence, successfully describing the parabolic behavior of the differential charge radii in $20 \leqslant N \leqslant 28$. We focus on its physical origin by decomposing it into radial and orbital contributions. The results are compared with those of the Skyrme plus normal pairing functional, which is considered as a representative of the usual EDFs. The enhancement of the differential charge radii in $N < 20$ with the Fayans functional, which contradicts the data, has the origin common to the parabolic behavior in $20 \leqslant N \leqslant 28$. It is important to describe both N regions simultaneously.

DOI: 10.1103/PhysRevC.110.054315

I. INTRODUCTION

Radius is a fundamental property of atomic nuclei. The radii of stable nuclei are proportional to $A^{1/3}$ in the first approximation, where A is the mass number, linked to the saturation of density [1]. This characteristic results from the balance between the attractions among the nucleons at low density and repulsion, which becomes dominant at high densities. The self-consistent mean-field or density functional theory (DFT) calculations have been developed and are now recognized as the standard approaches to the nuclear structure. Because nuclei are self-bound systems, self-consistent DFT calculations provide a suitable framework for studying nuclear radii. Conversely, an accurate description of the radii is fundamental to DFT because the density $\rho_t(\mathbf{r})$ ($t = n, p$) is usually taken as a principal variable [2], and the mean-square radius is the lowest-order moment of $\rho_t(\mathbf{r})$,

$$\langle r^2 \rangle_t = \frac{1}{N_t} \int d^3r\, r^2\, \rho_t(\mathbf{r}), \tag{1}$$

where N_t is the neutron or proton number (i.e., N or Z).

The nuclear charge radii are measured using electric probes [3], and their data are much less ambiguous than those obtained using hadronic probes. Owing to the recent developments in laser spectroscopy experiments [4,5], abundant data on the differential charge radii have been accumulated via isotope-shift measurements, and several intriguing results beyond the $A^{1/3}$ rule have been reported. The kinks at magic neutron numbers are among them: the kinks at $N = 126$ near Pb isotopes [6,7], at $N = 82$ in the Sn isotopes [8], and at $N = 28$ in the Ca and Ni isotopes [9,10]. Arguments linking the kinks to properties of nucleonic interactions or the energy density functional (EDF) have been given. In Refs. [11,12], the kinks are attributed to the spin-orbit interaction between the nucleons, which can be congenial to relativistic approaches [13]. Additional effects of density dependence of the spin-orbit interaction connected to three-nucleon interactions have been discussed [14–16]. In contrast, Fayans proposed an EDF with an extended form of the pairing functional [17,18], which has been claimed to play a significant role in kinks instead of the spin-orbit interactions [19].

Another interesting result has been observed for $^{40-48}$Ca. The charge radii of the even-N Ca nuclei vary parabolically as a function of N. This behavior is difficult to account for. A suggestion from the shell model is that the parabolic behavior may be a result of proton excitation across the $Z = 20$ core [20]. A correlation between charge radii and quadrupole collectivity have been discussed [21]. In contrast, the Fayans EDF reproduces parabolic behavior in self-consistent calculations that do not activate proton excitation across the $Z = 20$ core [18,19]. However, the even-odd staggering of the charge radii tends to be excessively strong when applying the Fayans EDF with parameters that accurately reproduced the parabola. Moreover, the behavior of the charge radii in the neutron-deficient region contradicts experimental data [22], which were argued in connection with the ℓs-closed nature of $N = 20$ and called *antikink* in Ref. [23].

*Contact author: inakura@gmail.com
†Contact author: hinohara@nucl.ph.tsukuba.ac.jp
‡Contact author: nakada@faculty.chiba-u.jp

We investigate the charge radii of Ca nuclei in the nuclear DFT framework. As mentioned earlier, the Fayans EDF has distinct characteristics that can describe the parabolic behavior of the charge radii in $20 \leqslant N \leqslant 28$. In Ref. [19], this property is indicated to originate in its specific pairing channel. Despite these remarkable results, it is unclear whether this picture is reasonable. We examine the radial and orbital contributions to the radii by comparing the results of the Fayans EDF with those of other EDFs, particularly a Skyrme EDF. This analysis may aid in discriminating between EDFs in future experiments.

II. METHOD

A. Skyrme and Fayans EDF

The Skyrme and Fayans EDFs are functionals of several local densities, commonly expressed in the form

$$E = \int d^3r\, \mathcal{E}(\mathbf{r}), \tag{2}$$

where $\mathcal{E}$ is composed of the kinetic-energy term with the averaged nucleon mass M, nuclear particle-hole, Coulomb, and pairing parts, as

$$\mathcal{E}(\mathbf{r}) = \sum_{t=\mathrm{n,p}} \frac{\tau_t(\mathbf{r})}{2M} + \mathcal{E}_{\mathrm{ph}}(\mathbf{r}) + \mathcal{E}_{\mathrm{Coul}}(\mathbf{r}) + \mathcal{E}_{\mathrm{pair}}(\mathbf{r}). \tag{3}$$

In this paper, we assume time-reversal symmetry, restricting ourselves to even-even nuclei. For a Skyrme EDF, the time-even particle-hole part of $\mathcal{E}$ consists of the volume, surface, and spin-orbit terms,

$$\mathcal{E}^{\mathrm{Sk}}_{\mathrm{ph}}[\rho,\tau,\mathbf{J}] = \mathcal{E}^{\mathrm{Sk}}_{\mathrm{v}}[\rho,\tau] + \mathcal{E}^{\mathrm{Sk}}_{\mathrm{s}}[\rho] + \mathcal{E}^{\mathrm{Sk}}_{\mathrm{ls}}[\rho,\mathbf{J}]; \tag{4}$$

$$\mathcal{E}^{\mathrm{Sk}}_{\mathrm{v}}[\rho,\tau] = \sum_{k=0,1} \left\{ C^{\rho}_k[\rho_0][\rho_k(\mathbf{r})]^2 + C^{\tau}_k \rho_k(\mathbf{r})\tau_k(\mathbf{r}) \right\}, \tag{5}$$

$$\mathcal{E}^{\mathrm{Sk}}_{\mathrm{s}}[\rho] = \sum_{k=0,1} C^{\Delta\rho}_k \rho_k(\mathbf{r})\Delta\rho_k(\mathbf{r}), \tag{6}$$

$$\mathcal{E}^{\mathrm{Sk}}_{\mathrm{ls}}[\rho,\mathbf{J}] = \sum_{k=0,1} C^{\nabla J}_k \rho_k(\mathbf{r})\nabla\cdot\mathbf{J}_k(\mathbf{r}), \tag{7}$$

where $\rho_k(\mathbf{r})$, $\tau_k(\mathbf{r})$, and $\mathbf{J}_k(\mathbf{r})$ are the local particle densities, kinetic densities, and spin-orbit densities [24] with $k = 0$ and 1 corresponding to the isoscalar and isovector parts, respectively, e.g., $\rho_0(\mathbf{r}) = \rho_{\mathrm{n}}(\mathbf{r}) + \rho_{\mathrm{p}}(\mathbf{r})$ and $\rho_1(\mathbf{r}) = \rho_{\mathrm{n}}(\mathbf{r}) - \rho_{\mathrm{p}}(\mathbf{r})$. The ρ_0-dependent coupling constant is given by $C^{\rho}_k[\rho_0] = C^{\rho}_k[0] + C^{\rho}_{kD}[\rho_0(\mathbf{r})]^{\alpha}$.

The particle-hole part of the Fayans EDF [17], which does not contain $\tau_k(\mathbf{r})$, is composed of the volume, surface, and spin-orbit parts,

$$\mathcal{E}^{\mathrm{Fy}}_{\mathrm{ph}}[\rho,\mathbf{J}] = \mathcal{E}^{\mathrm{Fy}}_{\mathrm{v}}[\rho] + \mathcal{E}^{\mathrm{Fy}}_{\mathrm{s}}[\rho] + \mathcal{E}^{\mathrm{Fy}}_{\mathrm{ls}}[\rho,\mathbf{J}]; \tag{8}$$

$$\mathcal{E}^{\mathrm{Fy}}_{\mathrm{v}}[\rho] = \frac{\epsilon_F \rho_{\mathrm{sat}}}{3} \left\{ a^{\mathrm{v}}_{+} \frac{1 - h^{\mathrm{v}}_{1+}[x_0(\mathbf{r})]^{\sigma}}{1 + h^{\mathrm{v}}_{2+}[x_0(\mathbf{r})]^{\sigma}} [x_0(\mathbf{r})]^2 + a^{\mathrm{v}}_{-} \frac{1 - h^{\mathrm{v}}_{1-} x_0(\mathbf{r})}{1 + h^{\mathrm{v}}_{2-} x_0(\mathbf{r})} [x_1(\mathbf{r})]^2 \right\}, \tag{9}$$

$$\mathcal{E}^{\mathrm{Fy}}_{\mathrm{s}}[\rho] = \frac{\epsilon_F \rho_{\mathrm{sat}}}{3} \frac{a^{\mathrm{s}}_{+} r_s^2 [\nabla x_0(\mathbf{r})]^2}{1 + h^{\mathrm{s}}_{+}[x_0(\mathbf{r})]^{\sigma} + h^{\mathrm{s}}_{\nabla} r_s^2 [\nabla x_0(\mathbf{r})]^2}, \tag{10}$$

$$\mathcal{E}^{\mathrm{Fy}}_{\mathrm{ls}}[\rho,\mathbf{J}] = \frac{4\epsilon_F r_s^2}{3\rho_{\mathrm{sat}}} [\kappa \rho_0(\mathbf{r})\nabla\cdot\mathbf{J}_0(\mathbf{r}) + \kappa' \rho_1(\mathbf{r})\nabla\cdot\mathbf{J}_1(\mathbf{r})]. \tag{11}$$

The density-dependent coupling constants in the volume and surface terms are given in a form analogous to the Padé approximant. The density $\rho_k(\mathbf{r})$ is used in terms of $x_k(\mathbf{r}) = \rho_k(\mathbf{r})/\rho_{\mathrm{sat}}$, normalized to the saturation density $\rho_{\mathrm{sat}} = 0.16\ \mathrm{fm}^{-3}$. The parameters ϵ_F and r_s are the Fermi energy and Wigner-Seitz radius, respectively, whose values are given in Appendix A. The volume term corresponds to substitution of the Skyrme coupling constants C^{ρ}_k for

$$C^{\rho}_0[\rho_0] = \frac{\epsilon_F a^{\mathrm{v}}_{+}}{3\rho_{\mathrm{sat}}} \frac{1 - h^{\mathrm{v}}_{1+}[x_0(\mathbf{r})]^{\sigma}}{1 + h^{\mathrm{v}}_{2+}[x_0(\mathbf{r})]^{\sigma}}, \tag{12}$$

$$C^{\rho}_1[\rho_0] = \frac{\epsilon_F a^{\mathrm{v}}_{-}}{3\rho_{\mathrm{sat}}} \frac{1 - h^{\mathrm{v}}_{1-} x_0(\mathbf{r})}{1 + h^{\mathrm{v}}_{2-} x_0(\mathbf{r})}. \tag{13}$$

The surface term of the Fayans EDF approximately corresponds to the isoscalar surface term of the Skyrme EDF that contains $\rho_0\Delta\rho_0$ but with density-dependent $C^{\Delta\rho}_0$. The isovector term proportional to $\rho_1\Delta\rho_1$ is not present in the Fayans surface term. The spin-orbit term of the Fayans EDF has the same functional form as the extended Skyrme EDF [12]. Two parameters κ and κ' are used, which are related to the Skyrme coupling constants as

$$C^{\nabla J}_0 = \frac{4\epsilon_F r_s^2}{3\rho_{\mathrm{sat}}}\kappa, \tag{14}$$

$$C^{\nabla J}_1 = \frac{4\epsilon_F r_s^2}{3\rho_{\mathrm{sat}}}\kappa'. \tag{15}$$

The Coulomb EDF is expressed as the sum of direct and exchange contributions

$$\mathcal{E}_{\mathrm{Coul}}[\rho] = \frac{e^2}{2}\rho_{\mathrm{p}}(\mathbf{r}) \int d^3r' \frac{\rho_{\mathrm{p}}(\mathbf{r}')}{|\mathbf{r} - \mathbf{r}'|} - \frac{3}{4}\left(\frac{3}{\pi}\right)^{\frac{1}{3}} e^2 [\rho_{\mathrm{p}}(\mathbf{r})]^{\frac{4}{3}} \{1 - h_{\mathrm{Coul}}[x_0(\mathbf{r})]^{\sigma}\}, \tag{16}$$

where the point-proton density $\rho_{\mathrm{p}}(\mathbf{r})$ is used instead of the charge density. The Coulomb exchange energy is evaluated using the Slater approximation, in addition to the Coulomb-nuclear correlation term controlled by the parameter h_{Coul}. In the Skyrme EDF, $h_{\mathrm{Coul}} = 0$.

The pairing functionals of the Skyrme and Fayans EDFs are

$$\mathcal{E}^{\mathrm{Sk}}_{\mathrm{pair}}[\rho,\tilde{\rho},\tilde{\rho}^*] = \sum_{t=\mathrm{n,p}} \frac{V_t}{4}\left[1 - \eta\frac{\rho_0(\mathbf{r})}{\rho_{\mathrm{pair}}}\right]|\tilde{\rho}_t(\mathbf{r})|^2, \tag{17}$$

$$\mathcal{E}^{\mathrm{Fy}}_{\mathrm{pair}}[\rho,\tilde{\rho},\tilde{\rho}^*] = \frac{2\epsilon_F}{3\rho_{\mathrm{sat}}} \left\{ f^{\xi}_{\mathrm{ex}} + h^{\xi}_{+}[x_{\mathrm{pair}}(\mathbf{r})]^{\gamma} + h^{\xi}_{\nabla} r_s^2 [\nabla x_{\mathrm{pair}}(\mathbf{r})]^2 \right\} \sum_{t=\mathrm{n,p}} |\tilde{\rho}_t(\mathbf{r})|^2 \tag{18}$$

with $x_{\rm pair}(\mathbf{r}) = \rho_0(\mathbf{r})/\rho_{\rm pair}$. It is customary to set $\rho_{\rm pair} = \rho_{\rm sat}$. In the Skyrme EDF, we use mixed-type pairing with $\eta = 1/2$. When $\gamma = 1$, the Fayans pairing parameters $f^{\xi}_{\rm ex}$ and h^{ξ}_{+} are related to the Skyrme pairing parameters as

$$V_t = \frac{8\epsilon_F}{3\rho_{\rm sat}} f^{\xi}_{\rm ex}, \tag{19}$$

$$\eta = -\frac{h^{\xi}_{+}}{f^{\xi}_{\rm ex}}. \tag{20}$$

However, the h^{ξ}_{∇} term, which depends on the derivative of the isoscalar density, is not present in the standard density-dependent pairing used with the Skyrme EDF.

The variational condition of the EDF results in the Hartree-Fock-Bogoliubov equation

$$\begin{pmatrix} h_t - \lambda_t & \tilde{h}_t \\ -\tilde{h}^*_t & -h^*_t + \lambda_t \end{pmatrix} \begin{pmatrix} \mathcal{U}_{\mu,t} \\ \mathcal{V}_{\mu,t} \end{pmatrix} = E_{\mu,t} \begin{pmatrix} \mathcal{U}_{\mu,t} \\ \mathcal{V}_{\mu,t} \end{pmatrix}. \tag{21}$$

The particle-hole and pairing parts of the local mean-field Hamiltonian are given by

$$h_t(\mathbf{r}; s', s) = -\nabla \cdot \frac{1}{2M^*_t(\mathbf{r})} \nabla \delta_{s's} + U_t(\mathbf{r}) \delta_{s's} + \frac{1}{i} (\nabla \times \hat{\boldsymbol{\sigma}}_{s's}) W_t(\mathbf{r}) \cdot \nabla, \tag{22}$$

$$\tilde{h}_t(\mathbf{r}; s', s) = \tilde{U}_t(\mathbf{r}) \delta_{s's}, \tag{23}$$

where $U_t(\mathbf{r})$, $W_t(\mathbf{r})$, and $\tilde{U}_t(\mathbf{r})$ are the central, spin-orbit (ℓs), and pairing potentials, respectively. $M^*_t(\mathbf{r})$ is the position-dependent effective mass, λ_t is the chemical potential, and $\hat{\boldsymbol{\sigma}}$ denotes the Pauli matrix. The potentials and effective masses are defined by the functional derivatives with respect to the corresponding densities:

$$U_t(\mathbf{r}) = \frac{\delta \mathcal{E}[\rho, \tau, \mathbf{J}, \tilde{\rho}, \tilde{\rho}^*]}{\delta \rho_t}, \tag{24}$$

$$W_t(\mathbf{r}) = \frac{\delta \mathcal{E}[\rho, \tau, \mathbf{J}, \tilde{\rho}, \tilde{\rho}^*]}{\delta (\nabla \cdot \mathbf{J}_t)}, \tag{25}$$

$$\tilde{U}_t(\mathbf{r}) = \frac{\delta \mathcal{E}[\rho, \tau, \mathbf{J}, \tilde{\rho}, \tilde{\rho}^*]}{\delta \tilde{\rho}^*_t}, \tag{26}$$

$$M^*_t(\mathbf{r}) = \frac{1}{2} \left(\frac{\delta \mathcal{E}[\rho, \tau, \mathbf{J}, \tilde{\rho}, \tilde{\rho}^*]}{\delta \tau_t} \right)^{-1}. \tag{27}$$

Equation (27) yields $M^*_t(\mathbf{r}) = M$ in the Fayans EDF. We define the pairing gap as a density-averaged pair potential,

$$\Delta_t = \frac{1}{N_t} \int d^3r \, \tilde{U}_t(\mathbf{r}) \rho_t(\mathbf{r}), \tag{28}$$

which will be used in Sec. III D.

Because it plays an important role in the charge radii in the Ca nuclei, we explicitly express the rearrangement term, the contribution to the central potential $U_t(\mathbf{r})$ from the pairing EDF [19], as

$$\frac{\delta \mathcal{E}^{\rm Sk}_{\rm pair}}{\delta \rho_t} = -\frac{\eta}{\rho_{\rm pair}} \sum_{t'={\rm n,p}} \frac{V_{t'}}{4} |\tilde{\rho}_{t'}(\mathbf{r})|^2, \tag{29}$$

$$\frac{\delta \mathcal{E}^{\rm Fy}_{\rm pair}}{\delta \rho_t} = \frac{2\epsilon_F}{3\rho_{\rm sat}} \left\{ \left[\frac{\gamma h^{\xi}_{+}}{\rho_{\rm pair}} [x_{\rm pair}(\mathbf{r})]^{\gamma-1} - \frac{2h^{\xi}_{\nabla} r_s^2}{\rho^2_{\rm pair}} \Delta\rho_0(\mathbf{r}) \right] \times \sum_{t'={\rm n,p}} |\tilde{\rho}_{t'}(\mathbf{r})|^2 - \frac{4h^{\xi}_{\nabla} r_s^2}{\rho^2_{\rm pair}} \sum_{t'={\rm n,p}} {\rm Re}\big[\tilde{\rho}^*_{t'}(\mathbf{r}) \nabla\rho_0(\mathbf{r}) \cdot \nabla \tilde{\rho}_{t'}(\mathbf{r})\big] \right\}. \tag{30}$$

The other terms of the potentials in the Fayans functionals are given in Appendix B.

B. Differential radii and densities

The mean-square radius of the point protons or neutrons is related to their density distributions via Eq. (1). In this paper, spherical symmetry is assumed for all the nuclei under investigation, and the densities are functions of $r = |\mathbf{r}|$. Although the charge radius and charge density are primarily dependent on the distribution of point protons, finite-size and relativistic corrections [25–27] are considered, as summarized in Appendix C.

The differences of the mean-square proton and charge radii between isotopes are denoted by

$$\delta\langle r^2\rangle^{A_0,A}_{\rm p} = \langle r^2\rangle_{\rm p}({}^{A}{\rm Ca}) - \langle r^2\rangle_{\rm p}({}^{A_0}{\rm Ca}), \tag{31}$$

$$\delta\langle r^2\rangle^{A_0,A}_{\rm ch} = \langle r^2\rangle_{\rm ch}({}^{A}{\rm Ca}) - \langle r^2\rangle_{\rm ch}({}^{A_0}{\rm Ca}) \tag{32}$$

with the reference nucleus ^{A_0}Ca. We also define the differential proton and charge densities as

$$\bar{\Delta}\rho^{A_0,A}_{\rm p}(r) := (4\pi r^2) r^2 [\rho_{\rm p}(r, {}^{A}{\rm Ca}) - \rho_{\rm p}(r, {}^{A_0}{\rm Ca})], \tag{33}$$

$$\bar{\Delta}\rho^{A_0,A}_{\rm ch}(r) := (4\pi r^2) r^2 [\rho_{\rm ch}(r, {}^{A}{\rm Ca}) - \rho_{\rm ch}(r, {}^{A_0}{\rm Ca})], \tag{34}$$

so that the integration of $\bar{\Delta}\rho^{A_0,A}_{\rm p}(r)$ [$\bar{\Delta}\rho^{A_0,A}_{\rm ch}(r)$] over r should be equal to $\delta\langle r^2\rangle^{A_0,A}_{\rm p}$ [$\delta\langle r^2\rangle^{A_0,A}_{\rm ch}$].

In Sec. III C, we consider the contribution of the individual proton orbit j to the proton radius and density. Hence, we consider the following quantities:

$$\bar{\Delta}\rho^{A_0,A}_{{\rm p},j}(r) := (4\pi r^2) r^2 \sum_m [|\varphi_{{\rm p},jm}(\mathbf{r}, {}^{A}{\rm Ca})|^2 - |\varphi_{{\rm p},jm}(\mathbf{r}, {}^{A_0}{\rm Ca})|^2], \tag{35}$$

where $\varphi_{{\rm p},jm}$ is the wave function of the proton single-particle (s.p.) orbit j with the magnetic quantum number m. For simplicity, we use the quantum number j also to represent the s.p. orbit. The sum of $\bar{\Delta}\rho^{A_0,A}_{{\rm p},j}(r)$ over the occupied orbits is $\bar{\Delta}\rho^{A_0,A}_{\rm p}(r)$ in Eq. (33). For the radii, we consider the isotopic difference in the root-mean-square proton radii of the

individual orbits,

$$\delta[\sqrt{\langle r^2\rangle}]^{A_0,A}_{\mathrm{p},j} := \left\{ \int_0^\infty dr\,(4\pi r^2) r^2 \times \frac{1}{2j+1} \sum_m |\varphi_{\mathrm{p},jm}(\mathbf{r},\ ^A\mathrm{Ca})|^2 \right\}^{1/2} - \left\{ \int_0^\infty dr\,(4\pi r^2) r^2 \times \frac{1}{2j+1} \sum_m |\varphi_{\mathrm{p},jm}(\mathbf{r},\ ^{A_0}\mathrm{Ca})|^2 \right\}^{1/2}. \quad (36)$$

C. Numerical settings

The coordinate-basis spherical code HFBRAD [28] is employed to compute the ground-state properties of the Ca nuclei. Although the code was originally adapted to the Skyrme EDF, we have also implemented the Fayans EDF in HFBRAD. We set the box size to $R_{\max} = 15$ fm and the lattice size to $\Delta r = 0.1$ fm. We apply a quasiparticle-energy cutoff of 15 MeV for the pairing channel of the Fayans EDF and 60 MeV for the Skyrme EDFs. The pairing strength for the mixed-type pairing of the Skyrme EDF is $V_{\mathrm{n}} = -283.7$ MeV fm^3, which is adjusted to the neutron gap of 1.245 MeV in ^{120}Sn [28].

The charge radii calculated with nonlocal EDFs are described in Sec. III A, for which the numerical methods described in Refs. [29,30] are applied.

III. RESULTS

A. Charge radii and charge densities

We have calculated the charge radii of even-N Ca isotopes with FaNDF^0 of the Fayans EDF [17] and several other EDFs: Skyrme SkM* [31], SLy4 [32], UNEDF1 [33], Gogny D1S [34], M3Y-type M3Y-P6 [16,35,36], and M3Y-P6a [14,16]. For comparison, the result of NL3, which is a relativistic EDF, is also obtained from Ref. [37]. Figure 1 shows the calculated differential charge radii $\delta\langle r^2\rangle^{40,A}_{\mathrm{ch}}$ of the even-N Ca nuclei and compares them with experimental data [3,9,22]. The charge radii calculated with SLy4 and UNEDF1 are analogous to those calculated with SkM*. Refer to Fig. 1(a) in Ref. [23] for the results of D1S and M3Y-P6a, which are similar to those of SkM* and M3Y-P6. No proton excitation across the $Z = 20$ core occurs in any calculation, and the N dependence is attributed primarily to the influence of neutrons on the proton s.p. wave functions. Only FaNDF^0 reproduces the parabolic structure of the charge radii in $^{40-48}$Ca, as discussed in Ref. [19], whereas other EDFs yield almost constant charge radii for $^{40-48}$Ca. In the neutron-deficient region, FaNDF^0 does not reproduce the charge radii at $N = 16$ and 18. The charge radii computed with FaNDF^0 in ^{36,38}Ca are larger than those in ^{40}Ca, although the experimental values decrease as N decreases. SkM* and M3Y-P6 reproduce the experimental data for ^{36,38}Ca fairly well. NL3 produces an almost constant charge radius in $^{36-48}$Ca. Consequently, no EDFs successfully reproduce the charge radii in the entire region of $^{36-48}$Ca. Reference [38] has shown that the perturbative effects of long- and short-range correlations do not produce a parabolic structure in $^{40-48}$Ca. As mentioned in Introduction, the influence of proton excitation across $Z = 20$ including shape fluctuation, which might be beyond the mean-field description, has been suggested for $^{42-46}$Ca in some studies [20,21].

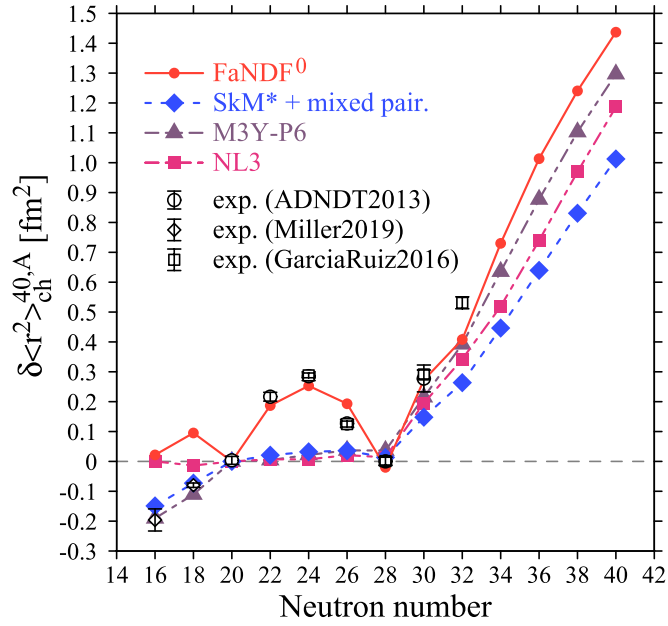

FIG. 1. Differential charge radii $\delta\langle r^2\rangle^{40,A}_{\mathrm{ch}}$ of even-N Ca isotopes calculated with FaNDF^0, SkM*, and M3Y-P6 are compared with the experimental data [3,9,22]. The charge radii calculated with NL3 are obtained from Ref. [37].

For neutron-rich nuclei with $N > 28$, all the EDFs reproduce and predict the steep growth of the charge radii with the neutron number, although the growth rate depends on the EDFs.

Because the Fayans EDF provides the characteristic behavior of the charge radii in $^{40-48}$Ca, we investigate what produces it in detail. In the following, we consider SkM* as a representative of the usual EDFs and compare its results with those of the Fayans EDF. While the Fayans-EDF parameters are further tuned in the functional Fy(Δr) [19] to reproduce the parabolic structure of the charge radii, we use the original parameter-set FaNDF^0 in this paper as their results are close to those of Fy(Δr).

B. Charge and point-proton density distributions

Figures 2(a) and 2(b) show the charge density distribution of ^{44}Ca, $\rho_{\mathrm{ch}}(r,\ ^{44}\mathrm{Ca})$, and its difference from that of ^{40}Ca, $\bar{\Delta}\rho^{A_0,A}_{\mathrm{ch}}(r)$ defined in Eq. (32), where $A_0 = 40$. The integrated value of $\bar{\Delta}\rho^{40,A}_{\mathrm{ch}}$ over r is equivalent to $\delta\langle r^2\rangle^{40,A}_{\mathrm{ch}}$, which has been shown in Fig. 1. Thus, $\bar{\Delta}\rho^{40,A}_{\mathrm{ch}}$ is the decomposition of $\delta\langle r^2\rangle^{40,A}_{\mathrm{ch}}$ as a function of r. The experimental data on $\bar{\Delta}\rho^{40,A}_{\mathrm{ch}}$ are obtained from Ref. [39], which are extracted from the densities fitted to the charge-form factors using the three-parameter Fermi (3pF) function. In ^{44}Ca, the neutrons gain pair correlation. In addition to the mixed-type pairing functional (17), the same pairing functional (18) as in FaNDF^0

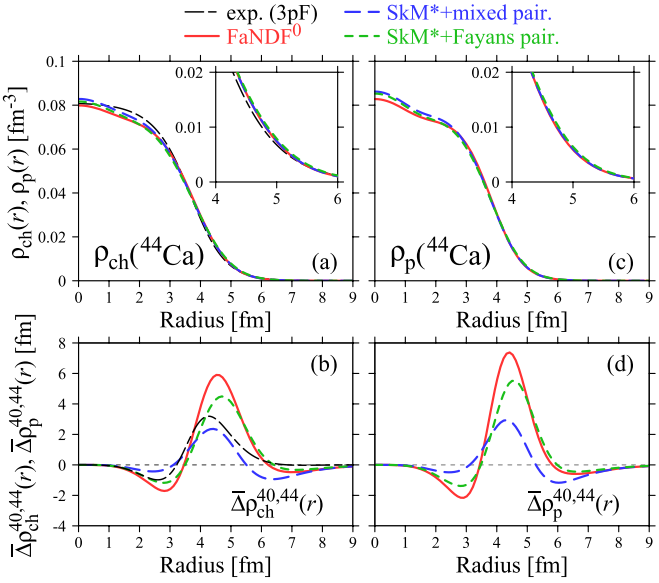

FIG. 2. Charge and point-proton density distributions of ^{44}Ca, $\rho_{ch/p}(r,\ ^{44}\text{Ca})$, and their differences from ^{40}Ca, $\bar{\Delta}\rho_{ch/p}^{40,44}(r)$. Those calculated with FaNDF^0 and SkM* are compared with the experimental data in the 3pF model.

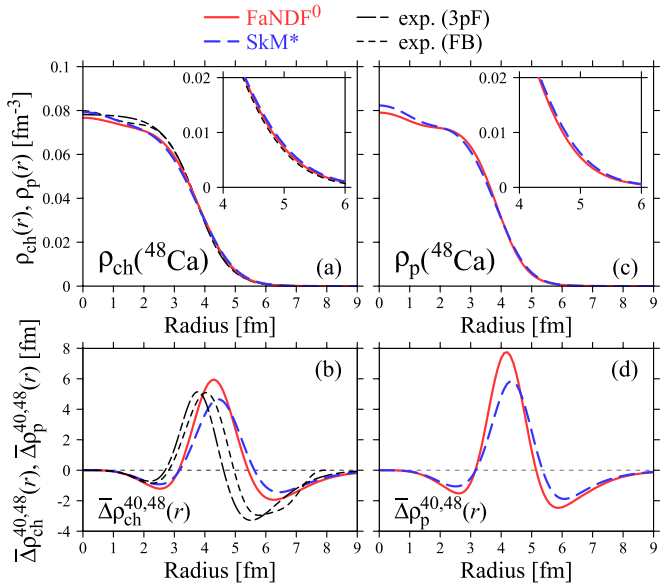

FIG. 3. Charge and point-proton density distributions of ^{48}Ca, $\rho_{ch/p}(r,\ ^{48}\text{Ca})$, and those differences from ^{40}Ca, $\bar{\Delta}\rho_{ch/p}^{40,48}(r)$. Those calculated with FaNDF^0 and SkM* are compared with the experimental data for charge radius distributions that are analyzed using the FB expansion and 3pF model.

[19] is applied to ^{44}Ca in combination with the particle-hole part of SkM* to investigate the influence of the pairing functional. Although the results for $\rho_{ch}(r,\ ^{44}\text{Ca})$ are not well distinguished among the EDFs [Fig. 2(a)], they are resolved in $\bar{\Delta}\rho_{ch}^{40,44}(r)$, i.e., the differences in charge densities from ^{40}Ca [Fig. 2(b)]. For $\bar{\Delta}\rho_{ch}^{40,44}$, all the calculations produce dips in the inner region of the nuclei and peaks in the surface region, which are qualitatively consistent with the experimental data (black dash-dotted line). Although the SkM* + mixed pairing (blue long-dashed line) has a peak height closer to the experimental data, it has a large negative contribution in the outer region of $r \approx 5$–8 fm, which offsets the positive contribution to $\langle r^2\rangle_{ch}$ in the surface region. FaNDF^0 (red solid line) provides a higher peak than the experimental data and has a negative contribution in the outer region, which the experimental data do not have. Consequently, FaNDF^0 reproduces the enhancement in the charge radius in ^{44}Ca well. Note that the experimental data for $\bar{\Delta}\rho_{ch}^{40,44}$ could contain systematic errors originating from the 3pF model. When the pairing functional is switched from the mixed-type functional to the Fayans functional (green dashed line) combined with the particle-hole part of SkM*, $\bar{\Delta}\rho_{ch}^{40,44}$ becomes similar to that of FaNDF^0. This confirms that Fayans pairing (18) is responsible for the parabolic behavior of charge radii in $^{40\text{–}48}$Ca.

Figures 3(a) and 3(b) show the calculated charge density distributions of ^{48}Ca, $\rho_{ch}(r,\ ^{48}\text{Ca})$, and their differences from those of ^{40}Ca, $\bar{\Delta}\rho_{ch}^{40,48}(r)$. They are also compared with experimental data [39] which were analyzed using the Fourier-Bessel (FB) expansion and 3pF model. The small deviation between the data extracted from the FB and 3pF models suggests that the model dependence in the experimental analyses is not significant. No pairing correlation is activated in the ground state of ^{48}Ca in the calculations in this paper. As in ^{44}Ca, both FaNDF^0 and SkM* produce similar charge-density distributions $\rho_{ch}(r)$ and are consistent with the experimental data [Fig. 3(a)]. Even for $\bar{\Delta}\rho_{ch}^{40,48}$ in Fig. 3(b), the results for FaNDF^0 and SkM* are similar with dips at $r =$ 2–3 fm, peaks in the surface region $r = 4$–5 fm, and sizable negative contributions in the outer region. These results are qualitatively consistent with the experimental data, although the positions of the dips and peaks are located outward by 0.5–1 fm compared with the experimental data. The negative values of $\bar{\Delta}\rho_{ch}^{40,48}$ in the outer region result in almost equal charge radii between ^{40}Ca and ^{48}Ca, as shown in Fig. 1. In contrast, Fig. 2(b) shows that the dip in $\bar{\Delta}\rho_{ch}^{40,44}$ in the outer region is shallow for the FaNDF^0 result. This is consistent with the experimental data and produces a parabolic structure of the charge radii, whereas SkM* provides negative values, as in $\bar{\Delta}\rho_{ch}^{40,48}$.

Although the corrections presented in Appendix C have been considered, $\rho_{ch}(r)$ is dominated by the point-proton density $\rho_p(r)$. Figures 2(c), 2(d) and 3(c), 3(d) depict $\rho_p(r)$ of ^{44,48}Ca and their differences from ^{40}Ca defined in Eq. (33). The above discussions on charge density distributions hold for the proton density distributions, although the amplitudes of $\bar{\Delta}\rho_{ch}^{40,A}(r)$ tend to be lower than those of $\bar{\Delta}\rho_p^{40,A}(r)$. The same holds for the $N < 20$ and $N > 28$ regions. In the following, we investigate the point-proton density distributions $\rho_p(r)$ and point-proton radii $\langle r^2\rangle_p$, rather than $\rho_{ch}(r)$ and $\langle r^2\rangle_{ch}$.

We now discuss the neutron-deficient nucleus, ^{38}Ca. As shown in Fig. 1, the measured charge radius of ^{38}Ca is smaller than that of ^{40}Ca, $\delta\langle r^2\rangle_{ch}^{38,40} = -0.080$ fm^2. SkM* and M3Y-P6 accurately reproduce $\delta\langle r^2\rangle_{ch}^{38,40}$, whereas FaNDF^0 overestimates it, yielding $\delta\langle r^2\rangle_{ch}^{38,40} = +0.095$ fm^2. We

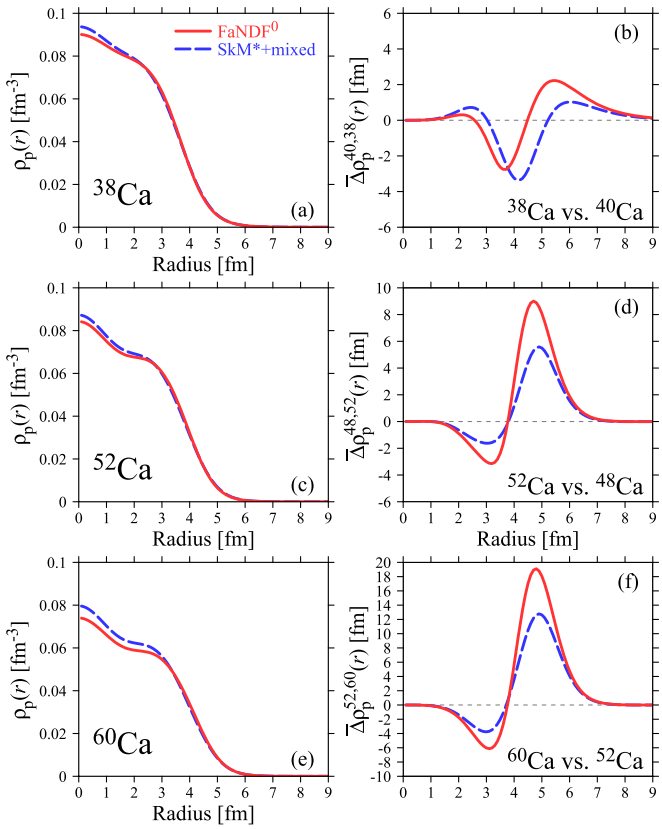

FIG. 4. Proton density distributions of (a) ^{38}Ca, (b) ^{52}Ca, and (c) ^{60}Ca calculated with FaNDF^0 and SkM* and their differences from the reference nuclei, which are set as ^{40}Ca for ^{38}Ca in (b), ^{48}Ca for ^{52}Ca (^{60}Ca) in (d) [(f)].

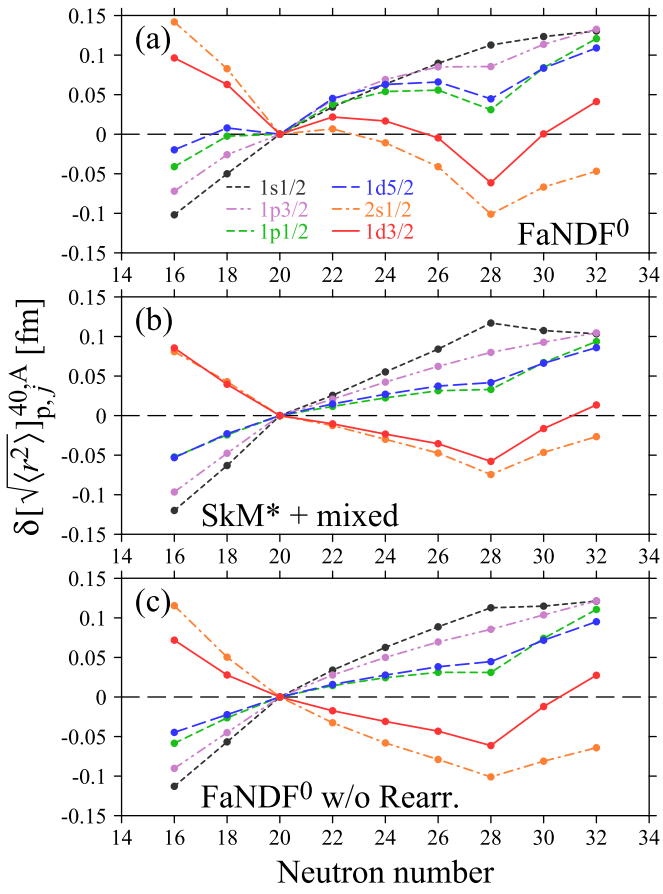

FIG. 5. Differences of proton singe-particle radii calculated with (a) FaNDF^0, (b) SkM*, and (c) FaNDF^0 after omitting the rearrangement term. See the text for details.

analyze the differential radius using the density distributions. Figures 4(a) and 4(b) show the proton density distributions and their differences from those in ^{40}Ca, defined in Eq. (33), which are calculated with FaNDF^0 and SkM*. Both FaNDF^0 and SkM* provide $\bar{\Delta}\rho_{\rm p}^{40,38}$ with dips of approximately $r = 4$ fm. However, FaNDF^0 has a significant peak in the outer region, which eliminates the contribution of the dip to $\delta\langle r^2\rangle_{\rm ch}^{38,40}$. The corresponding peak remains low in the SkM* results. Thus, as in the ^{44}Ca case, the N-dependence of the densities in the outer region causes a difference in charge radii between FaNDF^0 and SkM*.

For neutron-rich nuclei with $N > 28$, the charge radius increases monotonically both experimentally and theoretically, as shown in Fig. 1. The difference in the neutron-pairing functionals does not cause a qualitative difference in the charge radii, as long as N is restricted to be even. $\bar{\Delta}\rho_{\rm p}^{A_0,A}$ is comparable for FaNDF^0 and SkM*, as shown in Figs. 4(d) and 4(f), despite the difference in their amplitudes.

C. Orbital decomposition

Because $Z = 20$ is a magic number, the proton pair correlation is not active in any of the calculations presented here. The proton radius and density distribution can be decomposed into the contributions of the proton s.p. orbits that are filled at the $Z = 20$ magic number. Orbital decomposition may provide additional information on the N dependence of the radii, revealing the influence of the neutron occupation on specific orbits. To identify the orbital contributions to the differential proton radii, we show the differences in the radii of the individual proton s.p. orbits from those of ^{40}Ca, $\delta[\sqrt{\langle r^2\rangle}]_{{\rm p},j}^{40,A}$ in Eq. (36) as functions of N. The results obtained with FaNDF^0 and SkM* are presented in Figs. 5(a) and 5(b). A significant difference is observed between the FaNDF^0 and SkM* results corresponding to a difference in $\delta\langle r^2\rangle_{\rm ch}^{40,A}$. At $N = 22$, all the proton orbits have larger radii than those in ^{40}Ca in the FaNDF^0 results. In ^{44}Ca, $1d_{3/2}$ and $2s_{1/2}$ orbits shrink slightly, whereas the other proton orbits continue to expand. The differential radii of the proton orbit j are convex upwards in $^{40\text{–}48}$Ca, irrespective of j. All orbits except $2s_{1/2}$ make positive contributions to $\delta\langle r^2\rangle_{\rm p}^{40,44}$, resulting in the proton and charge radii in ^{44}Ca being larger than those in ^{40}Ca. Therefore, many orbits contribute coherently to the swelling of the point-proton and charge radii in ^{44}Ca. In particular, the sd-shell orbits, i.e., $1d_{5/2}$, $1d_{3/2}$, and $2s_{1/2}$, predominantly contribute to the convexity. Note that, in connection with the differential radii $\delta\langle r^2\rangle_{\rm p}^{A_0,A}$, the values in Fig. 5 must be multiplied by the occupation number, which is equal to the degeneracy of the orbit $(2j + 1)$. In ^{48}Ca, the proton $1d_{3/2}$ and $2s_{1/2}$ orbits become narrower than those in ^{40}Ca by 0.061

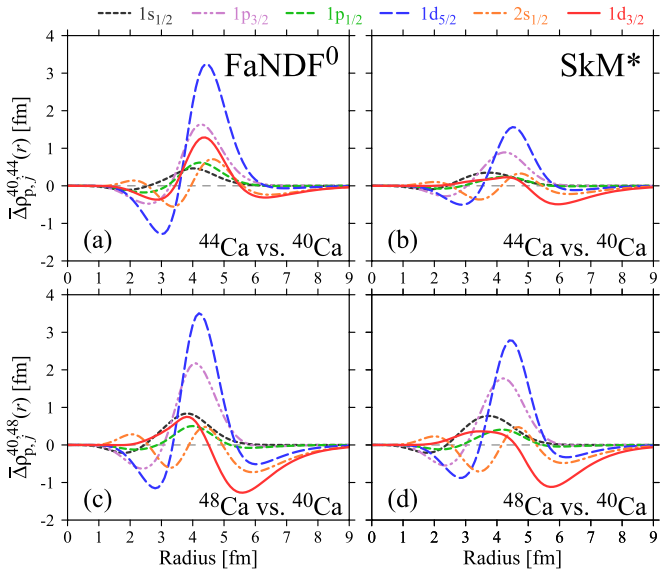

FIG. 6. Differences in proton density distributions of ^{44,48}Ca from ^{40}Ca, decomposed to proton orbits, $\bar{\Delta}\rho^{40,44}_{\mathrm{p},j}(r)$ and $\bar{\Delta}\rho^{40,48}_{\mathrm{p},j}(r)$. FaNDF^0 and SkM* are used.

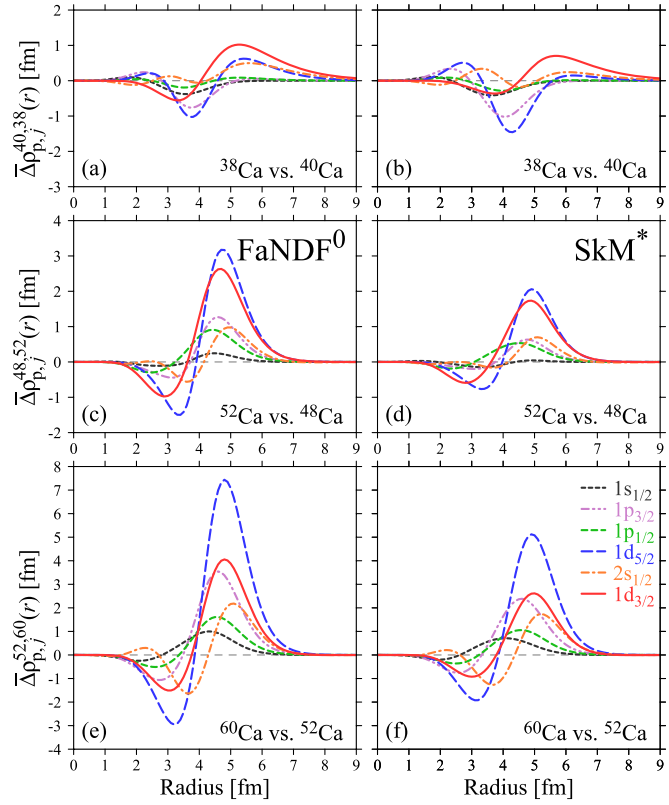

FIG. 7. Differences in proton density distributions between (a), (d) ^{40}Ca and ^{38}Ca, (b), (e) ^{48}Ca and ^{52}Ca, and (c), (f) ^{52}Ca and ^{60}Ca, decomposed to proton orbits. FaNDF^0 and SkM* are used.

and 0.101 fm, canceling the expansion of the other orbits and resulting in $\delta\langle r^2\rangle^{40,48}_{\mathrm{ch}} \approx 0$. Meanwhile, Fig. 5(b) shows that SkM* yields almost linear $\delta[\sqrt{\langle r^2\rangle}]^{40,A}_{\mathrm{p},j}$ for $^{40-48}$Ca. The proton radii calculated with SkM* do not vary significantly in $^{40-48}$Ca because the shrinkage of $1d_{3/2}$ and $2s_{1/2}$ cancels the spread of the other orbits, as observed for the charge radii in Fig. 1. When we employ FaNDF^0 by omitting the rearrangement terms of the neutron-pairing correlation in the central potential, $\delta\mathcal{E}_{\mathrm{pair}}/\delta\rho_t$, the behavior of $\delta[\sqrt{\langle r^2\rangle}]^{40,A}_{\mathrm{p},j}$ is similar to that calculated with SkM* (+ mixed pairing), as shown in Fig. 5(c) and Ref. [19]. The rearrangement term is crucial to reproducing the parabolic structure of the proton and charge radii in $^{40-48}$Ca. Note that the $1s_{1/2}$ and $2s_{1/2}$ orbits may easily mix in the mean-field calculations under spherical symmetry via a small off-diagonal component. The summed contributions from $1s_{1/2}$ and $2s_{1/2}$ remain small in all the cases, as shown in Fig. 5.

For ^{38}Ca, we observe that $\delta[\sqrt{\langle r^2\rangle}]^{40,38}_{\mathrm{p},1d_{5/2}}$ calculated with FaNDF^0 is positive, in contrast to those calculated with SkM* and without the rearrangement term. Moreover, $\delta[\sqrt{\langle r^2\rangle}]^{40,38}_{\mathrm{p},1p_{1/2}}$ almost vanishes in the FaNDF^0 result, being significant in providing a positive $\delta\langle r^2\rangle^{40,38}_{\mathrm{ch}}$ in Fig. 1, whereas those calculated with SkM* and without the rearrangement term are significantly negative.

We then analyze the radial contribution of each proton orbit to the differential proton radii. Figure 6 shows the differences of proton density distributions of ^{44,48}Ca from ^{40}Ca that are decomposed into the proton s.p. orbits, $\bar{\Delta}\rho^{40,44}_{\mathrm{p},j}(r)$ and $\bar{\Delta}\rho^{40,48}_{\mathrm{p},j}(r)$ in Eq. (35), calculated with FaNDF^0 and SkM*. In the FaNDF^0 results for ^{44}Ca, all proton-density differences except for the $s_{1/2}$ orbits have shallow dips in the inner region and high peaks in the surface region. The $1d_{3/2}$ and $2s_{1/2}$ orbits have small negative values in the outer region. The radial structure of $\bar{\Delta}\rho^{40,44}_{\mathrm{p},j}$ accounts for $\delta[\sqrt{\langle r^2\rangle}]^{40,44}_{\mathrm{p},j}$. Differences are observed between $\bar{\Delta}\rho^{40,48}_{\mathrm{p},j}$ and $\bar{\Delta}\rho^{40,44}_{\mathrm{p},j}$. Compared with $\bar{\Delta}\rho^{40,44}_{\mathrm{p},j}$, the peak positions of $\bar{\Delta}\rho^{40,48}_{\mathrm{p},j}$ of each orbit in the surface region shift inward by 0.2–0.3 fm, and the peak heights change by 0.1–0.5 fm. The most prominent difference is that $\bar{\Delta}\rho^{40,48}_{\mathrm{p},1d_{3/2}}$ and $\bar{\Delta}\rho^{40,48}_{\mathrm{p},2s_{1/2}}$ are sizably negative in the outer region, which diminishes the proton s.p. radii of the $1d_{3/2}$ and $2s_{1/2}$ orbits by 0.061 and 0.101 fm, respectively, as shown in Fig. 5(a). $\bar{\Delta}\rho^{40,48}_{\mathrm{p},1d_{5/2}}$ is also non-negligibly negative in the outer region. These shrinkages in the proton orbitals make the proton and charge radii of ^{48}Ca smaller than those of ^{44}Ca.

The shapes of $\bar{\Delta}\rho^{40,48}_{\mathrm{p},j}(r)$ calculated with SkM* are similar to those calculated with FaNDF^0. In ^{44}Ca, $\bar{\Delta}\rho^{40,44}_{\mathrm{p},j}(r)$ have smaller amplitudes than FaNDF^0. For SkM*, the shapes of $\bar{\Delta}\rho^{40,44}_{\mathrm{p},j}(r)$ are analogous to those of $\bar{\Delta}\rho^{40,48}_{\mathrm{p},j}(r)$ but with different scales. Therefore, the charge radii of ^{40,44,48}Ca calculated with SkM* are similar.

Figures 7(a) and 7(b) show $\bar{\Delta}\rho^{40,38}_{\mathrm{p},j}(r)$. As shown in Fig. 4(b), FaNDF^0 yields a large and positive $\bar{\Delta}\rho^{40,38}_{\mathrm{p}}(r)$ in the outer region. The $1d_{5/2}$, $1d_{3/2}$, and $2s_{1/2}$ orbits primarily make the difference from the SkM* result. This is similar to $\bar{\Delta}\rho^{40,44}_{\mathrm{p}}(r)$, regarding the significance of sd-shell orbits.

Figures 7(c)–7(f) show that all proton orbits coherently contribute in the surface to the outer region in the neutron-rich Ca nuclei, increasing the differential radii.

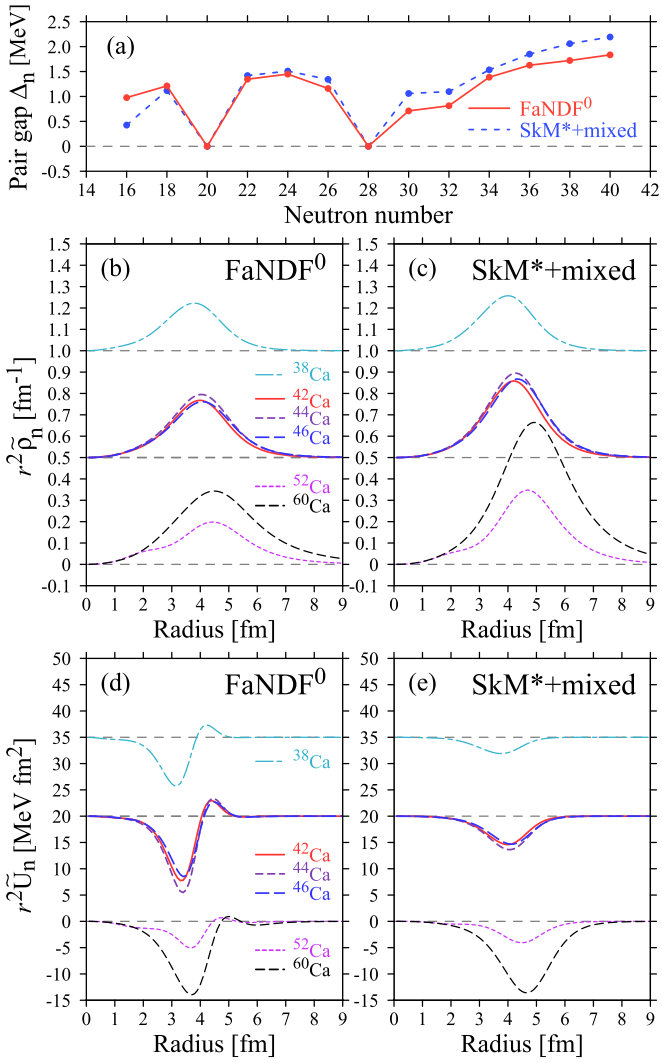

FIG. 8. Neutron pairing gaps Δ_n, neutron pair densities $r^2\tilde{\rho}_n$, and neutron pairing potentials $r^2\tilde{U}_n$ of even-N Ca nuclei, calculated with FaNDF^0 and SkM*. In (b)–(e), the curves are grouped and vertically shifted.

D. Difference in potentials

The neutron-pairing correlation is the key to producing a parabolic structure of charge radii in $^{40-48}$Ca in the Fayans EDF results. Figure 8 compares the neutron pairing gaps Δ_n, neutron pair density $r^2\tilde{\rho}_n$, and neutron pair potentials $r^2\tilde{U}_n$ in the Ca isotopes calculated with FaNDF^0 and SkM* (+ mixed pairing). The FaNDF^0 and SkM* functionals provide comparable pairing gaps. The neutron pair density distributions $r^2\tilde{\rho}_n$ in $^{42-46}$Ca are not significantly different, except that the peaks of $r^2\tilde{\rho}_n$ of SkM* are higher than those of FaNDF^0 and are located outward by 0.2–0.3 fm. However, a notable difference exists in the neutron pair potentials $r^2\tilde{U}_n$. Whereas SkM* yields valleys of $r^2\tilde{U}_n$ at $r \approx 4.1$ fm, FaNDF^0 yields valleys at $r \approx 3.4$ fm and bumps at $r \approx 4.5$ fm in $^{42-46}$Ca with nodes in the surface region $r \approx 4$ fm that SkM* does not produce. Moreover, the pair potential $r^2\tilde{U}_n$ of FaNDF^0 vanishes immediately beyond the bump, although $r^2\tilde{U}_n$ of

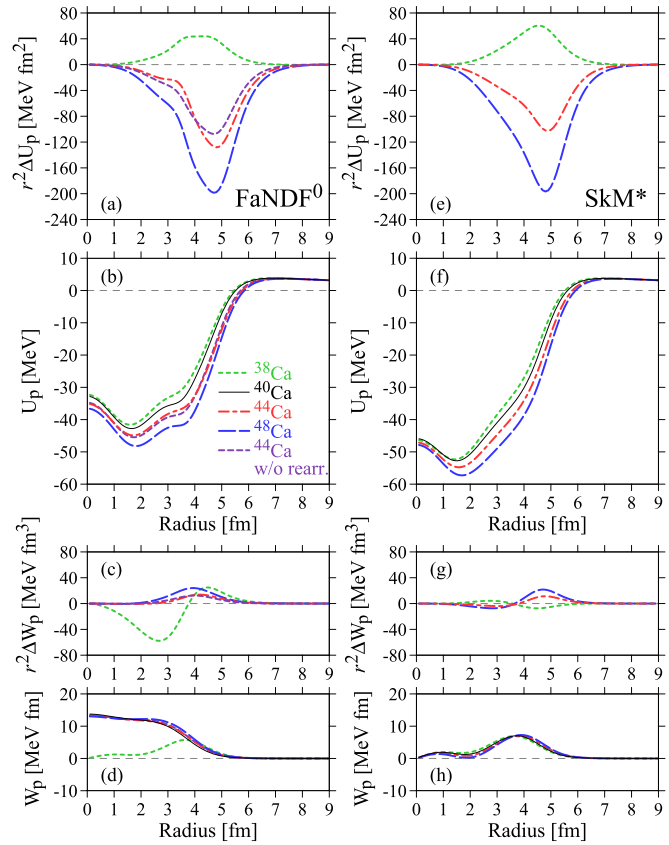

FIG. 9. Proton central potential U_p and ℓs potential W_p calculated with FaNDF^0 and SkM*, and those differences from ^{40}Ca.

SkM* varies gradually. This difference should result from the pairing functionals in Eqs. (17) and (18). It is worth noting that this difference is also observed in the $N < 20$ region. In the $N > 28$ region, a similar difference exists, but is less conspicuous.

Neutron pairing correlations affect the proton potential through the rearrangement term $\delta\mathcal{E}_{\rm pair}/\delta\rho_p$. If we omit the rearrangement term $\delta\mathcal{E}_{\rm pair}/\delta\rho_p$ in the proton central potential, the differences in the proton s.p. radii calculated with FaNDF^0 become similar to those calculated with SkM* (+ mixed pairing), as shown in Fig. 5(c). Figure 9 shows the proton central potential U_p and proton ℓs potential W_p of ^{40,44,48}Ca, as well as the differences in the potentials from ^{40}Ca, $r^2\Delta U_p^{40,A} := r^2[U_p(^A\mathrm{Ca}) - U_p(^{40}\mathrm{Ca})]$ and $r^2\Delta W_p^{40,A} := r^2[W_p(^A\mathrm{Ca}) - W_p(^{40}\mathrm{Ca})]$. $U_p(^{44}\mathrm{Ca})$ and $r^2\Delta U_p^{40,44}$ after omitting the rearrangement term are also plotted for reference. Rather than U_p itself, the difference between FaNDF^0 and SkM* in $r^2\Delta U_p^{40,A}$ is more relevant to $\delta\langle r^2\rangle_{{\rm ch}/p}^{40,A}$ under discussion. $r^2\Delta U_p^{40,44}$ of FaNDF^0 [red dot-dashed line in Fig. 9(a)] suddenly changes its slope at $r \approx 3.5$ fm and has a valley at $r \approx 4.7$ fm, corresponding to the bottom and top of $r^2\tilde{U}_n$ in Fig. 8. This structure of $r^2\Delta U_p^{40,44}$ causes the dip and peak of $\bar{\Delta}\rho_{{\rm ch}/p}^{40,44}(r)$ to be more conspicuous than those of SkM* in Fig. 2. Beyond the valley region, $r^2\Delta U_p^{40,44}$ of FaNDF^0 damps more slowly than that of SkM*, by which

the dip in $\bar{\Delta}\rho_{\rm p}^{40,44}(r)$ in the outer region becomes shallow, as shown in Fig. 2. If the rearrangement term $\delta\mathcal{E}_{\rm pair}/\delta\rho_{\rm p}$ is omitted (purple dashed line), the slope change in $r^2\Delta U_{\rm p}^{40,44}$ at $r \approx 3.5$ fm becomes milder. $\bar{\Delta}\rho_{\rm p}^{40,44}(r)$ of FaNDF^0 resembles that of SkM*, and the $\delta[\sqrt{\langle r^2\rangle}]_{p,j}^{40,44}$ values become similar to those of SkM*, as shown in Fig. 5. For the ℓs potentials, $W_{\rm p}$ hardly changes at $20 \leqslant N \leqslant 28$, and $\Delta W_{\rm p}^{40,A}$ has much smaller amplitudes than $\Delta U_{\rm p}^{40,A}$. Thus, the influence of the ℓs potential $\Delta W_{\rm p}^{40,A}$ on the proton and charge radii is insignificant.

The neutron pair density $r^2\tilde{\rho}_{\rm n}$ and neutron pair potential $r^2\tilde{U}_{\rm n}$ in ^{38}Ca are analogous to those in $^{42\text{–}46}$Ca [Fig. 8(d)]. If we omit the rearrangement term $\delta\mathcal{E}_{\rm pair}/\delta\rho_{\rm p}$ from the proton central potential of FaNDF^0, the calculated charge radius is close to the experimental value $\delta\langle r^2\rangle_{\rm ch}^{38,40} = -0.085$ fm^2. We further confirm that the neutron-pairing functional of the Fayans EDF, which looks favorable for the charge radii in $^{40\text{–}48}$Ca, simultaneously overestimates the charge radius in ^{38}Ca.

For the proton central potential, $r^2\Delta U_{\rm p}^{40,38}$ has a positive sign, opposite to $r^2\Delta U_{\rm p}^{40,44}$. Apart from the difference in sign, the connection between $r^2\Delta U_{\rm p}^{40,38}$ and $r^2\tilde{U}_{\rm n}$ in Fig. 8 is analogous to the case of $r^2\Delta U_{\rm p}^{40,44}$ discussed earlier. The positions of the sudden change in the slope and peak of $r^2\Delta U_{\rm p}^{40,38}$ correspond to the bottom and top of $r^2\tilde{U}_{\rm n}$, deriving $\bar{\Delta}\rho_{\rm p}^{40,38}(r)$ in Fig. 4. The slope of $r^2\Delta U_{\rm p}^{40,38}$ of FaNDF^0 changes at $r \approx 3.5$ fm, and a plateau begins. This behavior is not observed in $r^2\Delta U_{\rm p}^{40,38}$ of SkM*. The position of this slope change coincides with the minimum value of $\bar{\Delta}\rho_{\rm p}^{40,38}(r)$. Owing to its plateau structure, the peak in $r^2\Delta U_{\rm p}^{40,38}$ of FaNDF^0 is lower than that of SkM*, making the valley of $\bar{\Delta}\rho_{\rm p}^{40,38}(r)$ shallower and its maximum at $r \approx 5$ fm larger.

IV. SUMMARY AND DISCUSSIONS

We have investigated the charge and point-proton radii of Ca nuclei in the DFT framework. We reconfirm that the Fayans EDF provides a parabolic N dependence in the differential charge radii of $20 \leqslant N \leqslant 28$, which is compatible with experimental data owing to its unique pairing channels. By decomposing the charge and proton radii into radial and orbital contributions and giving special attention to the differential values from a reference nucleus, primarily ^{40}Ca, we analyze how the Fayans EDF provides a specific N dependence of the radii. The results of the Fayans EDF (FaNDF^0) are compared with those of SkM*, which is a representative EDFs with a normal pairing channel.

The characteristic N dependence in the $20 \leqslant N \leqslant 28$ region produced by the Fayans EDF is traced back to the neutron pair potential, which exhibits nodal behavior with a valley at a smaller r than the pair potential of the SkM*, a bump in the surface region, and abrupt damping beyond it. This influences the central part of the proton s.p. potential, as indicated by $r^2\Delta U_{\rm p}^{40,A}$, and the proton and charge densities. In terms of the orbitals, the influence on the sd-shell orbits, $1d_{3/2}$ and $2s_{1/2}$ in particular, is significant. However, although the N dependence of the charge radii is compatible with the experimental data for $20 \leqslant N \leqslant 28$, the same mechanism results in an erroneous enhancement of the charge radii in the $N < 20$ region. Studies have also suggested the role of proton excitation across the magic number $Z = 20$ for the charge radii of $^{40\text{–}48}$Ca. To determine the correct physics of the charge radii in the Ca isotopes, it is important to discuss ^{36,38}Ca simultaneously. It would be interesting to obtain the radial or orbital information of the radii in future experiments.

We also investigate the N dependence of the charge and proton radii in the neutron-rich region. Irrespective of the EDFs with no qualitatively apparent distinction, a steady increase in the charge radii with increasing N is predicted, although a quantitative difference is observed.

TABLE I. Parameters of FaNDF^0.

$a_+^{\rm v}$	−9.559	σ	1/3
$h_{1+}^{\rm v}$	0.633	$h_{\rm Coul}$	0.941
$h_{2+}^{\rm v}$	0.131	κ	0.19
$a_-^{\rm v}$	4.428	κ'	0
$h_{1-}^{\rm v}$	0.250	$f_{\rm ex}^{\xi}$	−2.8
$h_{2-}^{\rm v}$	1.300	h_+^{ξ}	2.8
$a_+^{\rm s}$	0.600	h_∇^{ξ}	2.2
$h_\nabla^{\rm s}$	0.440	γ	1

ACKNOWLEDGMENTS

The authors are grateful to T. Naito for useful comments and discussions. This work was supported by the JSPS KAKENHI (Grants No. JP19KK0343, No. JP20K03964, and No. JP24K07012) and the JST ERATO (Grant No. JPMJER2304).

APPENDIX A: FaNDF^0 PARAMETER

The parameters of FaNDF^0 [17] are summarized here. In this Appendix, we define all the parameters in terms of $\rho_{\rm sat} = 0.16$ fm^{-3}.[1] The Wigner-Seitz radius is given by

$$r_s = \left(\frac{3}{4\pi\rho_{\rm sat}}\right)^{\frac{1}{3}} = 1.143\,\text{fm}. \tag{A1}$$

The Fermi momentum and energy are

$$k_F = \left(\frac{3\pi^2\rho_{\rm sat}}{2}\right)^{\frac{1}{3}} = 1.333\,\text{fm}^{-1}, \tag{A2}$$

$$\epsilon_F = \frac{\hbar^2 k_F^2}{2m} = 36.846\,\text{MeV}. \tag{A3}$$

In several references, the inverse density of state is defined as

$$c_0 = \frac{4\epsilon_F}{3\rho_{\rm sat}} = 307.049\,\text{MeV fm}^3. \tag{A4}$$

Table I summarizes the values of the dimensionless parameters of FaNDF^0.

[1] In the original reference [17], the saturation density $\rho_{\rm sat}$ is denoted as $2\rho_0$.

APPENDIX B: FAYANS POTENTIAL

Here, we provide an explicit form for the central, ℓs and pairing potentials in the Fayans EDF. Note that $M_t^*(\mathbf{r}) = M$. The neutron and proton central potentials are given by

$$\begin{aligned} U_t(\mathbf{r}) &= \frac{\delta\mathcal{E}[\rho,\mathbf{J},\tilde{\rho},\tilde{\rho}^*]}{\delta\rho_t} \\ &= \frac{\delta\mathcal{E}_{\rm v}^{\rm Fy}[\rho]}{\delta\rho_t} + \frac{\delta\mathcal{E}_{\rm s}^{\rm Fy}[\rho]}{\delta\rho_t} + \frac{\delta\mathcal{E}_{\rm ls}^{\rm Fy}[\rho,\mathbf{J}]}{\delta\rho_t} \\ &\quad + \frac{\delta\mathcal{E}_{\rm Coul}[\rho]}{\delta\rho_t} + \frac{\delta\mathcal{E}_{\rm pair}^{\rm Fy}[\rho,\tilde{\rho},\tilde{\rho}^*]}{\delta\rho_t}, \end{aligned} \tag{B1}$$

where

$$\begin{aligned} \frac{\delta\mathcal{E}_{\rm v}^{\rm Fy}}{\delta\rho_t} &= \frac{\epsilon_F}{3}a_+^{\rm v}\Bigg[-\sigma\frac{h_{1+}^{\rm v}+h_{2+}^{\rm v}}{\left\{1+h_{2+}^{\rm v}[x_0(\mathbf{r})]^\sigma\right\}^2}[x_0(\mathbf{r})]^{\sigma+1} \\ &\quad + 2\frac{1-h_{1+}^{\rm v}[x_0(\mathbf{r})]^\sigma}{1+h_{2+}^{\rm v}[x_0(\mathbf{r})]^\sigma}x_0(\mathbf{r})\Bigg] \\ &\quad + \frac{\epsilon_F}{3}a_-^{\rm v}\Bigg[-\frac{h_{1-}^{\rm v}+h_{2-}^{\rm v}}{\left[1+h_{2-}^{\rm v}x_0(\mathbf{r})\right]^2}[x_1(\mathbf{r})]^2 \\ &\quad \pm 2\frac{1-h_{1-}^{\rm v}x_0(\mathbf{r})}{1+h_{2-}^{\rm v}x_0(\mathbf{r})}x_1(\mathbf{r})\Bigg], \end{aligned} \tag{B2}$$

$$\begin{aligned} \frac{\delta\mathcal{E}_{\rm s}^{\rm Fy}}{\delta\rho_t} &= -\frac{\epsilon_F}{3}\frac{\sigma h_+^{\rm s}a_+^{\rm s}r_s^2[\nabla x_0(\mathbf{r})]^2[x_0(\mathbf{r})]^{\sigma-1}}{\left\{1+h_+^{\rm s}[x_0(\mathbf{r})]^\sigma+h_\nabla^{\rm s}r_s^2[\nabla x_0(\mathbf{r})]^2\right\}^2} \\ &\quad - \frac{2\epsilon_F}{3\rho_{\rm sat}}\frac{a_+^{\rm s}r_s^2\{1+h_+^{\rm s}[x_0(\mathbf{r})]^\sigma\}\Delta\rho_0(\mathbf{r})}{\left\{1+h_+^{\rm s}[x_0(\mathbf{r})]^\sigma+h_\nabla^{\rm s}r_s^2[\nabla x_0(\mathbf{r})]^2\right\}^2} \\ &\quad + \frac{\epsilon_F a_+^{\rm s}r_s^2h_+^{\rm s}\sigma[x_0(\mathbf{r})]^{\sigma-1}[\nabla\rho_0(\mathbf{r})]^2}{3\rho_{\rm sat}^2} \\ &\quad \times\frac{1+h_+^{\rm s}[x_0(\mathbf{r})]^\sigma-3h_\nabla^{\rm s}r_s^2[\nabla x_0(\mathbf{r})]^2}{\left\{1+h_+^{\rm s}[x_0(\mathbf{r})]^\sigma+h_\nabla^{\rm s}r_s^2[\nabla x_0(\mathbf{r})]^2\right\}^3} \\ &\quad + \frac{8\epsilon_F}{3\rho_{\rm sat}^3}\frac{a_+^{\rm s}h_\nabla^{\rm s}r_s^4\{1+h_+^{\rm s}[x_0(\mathbf{r})]^\sigma\}}{\left\{1+h_+^{\rm s}[x_0(\mathbf{r})]^\sigma+h_\nabla^{\rm s}r_s^2[\nabla x_0(\mathbf{r})]^2\right\}^3} \\ &\quad \times\sum_{ab}[\nabla_a\rho_0(\mathbf{r})][\nabla_b\rho_0(\mathbf{r})][\nabla_a\nabla_b\rho_0(\mathbf{r})], \end{aligned} \tag{B3}$$

$$\frac{\delta\mathcal{E}_{\rm ls}^{\rm Fy}}{\delta\rho_t} = \frac{4\epsilon_F r_s^2}{3\rho_{\rm sat}}[\kappa\nabla\cdot\mathbf{J}_0(\mathbf{r}) \pm \kappa'\nabla\cdot\mathbf{J}_1(\mathbf{r})], \tag{B4}$$

$$\begin{aligned} \frac{\delta\mathcal{E}_{\rm Coul}}{\delta\rho_{\rm p}} &= \frac{e^2}{2}\int d^3r'\frac{\rho_{\rm p}(\mathbf{r}')}{|\mathbf{r}-\mathbf{r}'|} \\ &\quad - \left(\frac{3}{\pi}\right)^{\frac{1}{3}}e^2[\rho_{\rm p}(\mathbf{r})]^{\frac{1}{3}}\{1-h_{\rm Coul}[x_0(\mathbf{r})]^\sigma\} \\ &\quad + \sigma\frac{h_{\rm Coul}}{\rho_{\rm sat}}\frac{3}{4}\left(\frac{3}{\pi}\right)^{\frac{1}{3}}e^2[\rho_{\rm p}(\mathbf{r})]^{\frac{4}{3}}[x_0(\mathbf{r})]^{\sigma-1}, \end{aligned} \tag{B5}$$

$$\frac{\delta\mathcal{E}_{\rm Coul}}{\delta\rho_{\rm n}} = \sigma\frac{h_{\rm Coul}}{\rho_{\rm sat}}\frac{3}{4}\left(\frac{3}{\pi}\right)^{\frac{1}{3}}e^2[\rho_{\rm p}(\mathbf{r})]^{\frac{4}{3}}[x_0(\mathbf{r})]^{\sigma-1}. \tag{B6}$$

The last term in Eq. (B1) is the pairing rearrangement term in Eq. (30). The ℓs potential is given by

$$W_t(\mathbf{r}) = \frac{\delta\mathcal{E}_{\rm ls}^{\rm Fy}}{\delta(\nabla\cdot\mathbf{J}_t)} = \frac{4\epsilon_F r_s^2}{3\rho_{\rm sat}}[\kappa\rho_0(\mathbf{r}) \pm \kappa'\rho_1(\mathbf{r})]. \tag{B7}$$

A positive (negative) sign is used for the neutron (proton) potential in Eqs. (B2), (B4), and (B7).

The pairing potential is given by

$$\begin{aligned} \tilde{U}_t(\mathbf{r}) &= \frac{\delta\mathcal{E}_{\rm pair}^{\rm Fy}[\rho,\tilde{\rho},\tilde{\rho}^*]}{\delta\tilde{\rho}_t^*} \\ &= \frac{4\epsilon_F}{3\rho_{\rm sat}}\left[f_{\rm ex}^\xi + h_+^\xi[x_{\rm pair}(\mathbf{r})]^\gamma + h_\nabla^\xi r_s^2[\nabla x_{\rm pair}(\mathbf{r})]^2\right]\tilde{\rho}_t(\mathbf{r}). \end{aligned} \tag{B8}$$

APPENDIX C: CHARGE DENSITY

The charge density is computed from the convoluted single-nucleon densities [26]

$$\rho_{\rm ch}(\mathbf{r}) = \sum_{t={\rm n,p}}[\rho_{ct}(\mathbf{r}) + \omega_{ct}(\mathbf{r})], \tag{C1}$$

where

$$\rho_{ct}(\mathbf{r}) = \int d^3x\int\frac{d^3q}{(2\pi)^3}e^{i\mathbf{q}\cdot(\mathbf{x}-\mathbf{r})}G_{Et}(q^2)\rho_t(\mathbf{x}), \tag{C2}$$

$$\omega_{ct}(\mathbf{r}) = \int d^3x\int\frac{d^3q}{(2\pi)^3}e^{i\mathbf{q}\cdot(\mathbf{x}-\mathbf{r})}F_{2t}(q^2)\omega_t(\mathbf{x}). \tag{C3}$$

In Eq. (C2), $\rho_t(\mathbf{r})$ is the point-proton or point-neutron density. We use the nonrelativistic form of the spin-orbit density in Eq. (C3),

$$\omega_t(\mathbf{r}) = -\frac{\mu_t'\hbar^2}{2(Mc)^2}\nabla\cdot\mathbf{J}_t(\mathbf{r}), \tag{C4}$$

where $Mc^2 = 939$ MeV is the average nucleon mass, and μ_t' is the anomalous magnetic moment, related to the nucleon magnetic moments $\mu_{\rm n} = -1.913$ and $\mu_{\rm p} = 2.793$ as $\mu_{\rm n}' = \mu_{\rm n}$ and $\mu_{\rm p}' = \mu_{\rm p} - 1$. The Sachs and Pauli form factors are selected as follows:

$$G_{E{\rm n}}(q^2) = \frac{1}{(1+r_+^2q^2/12)^2} - \frac{1}{(1+r_-^2q^2/12)^2}, \tag{C5}$$

$$G_{E{\rm p}}(q^2) = \frac{1}{\left(1+r_{\rm p}^2q^2/12\right)^2}, \tag{C6}$$

$$F_{2{\rm n}}(q^2) = \frac{G_{E{\rm p}}(q^2) - G_{E{\rm n}}(q^2)/\mu_{\rm n}'}{1+q^2/4M^2}, \tag{C7}$$

$$F_{2{\rm p}}(q^2) = \frac{G_{E{\rm p}}(q^2)}{1+q^2/4M^2}, \tag{C8}$$

and $r_{\rm p} = 0.84$ fm [40] and $r_\pm^2 = (0.830)^2 \mp 0.058$ fm^2 [41] are adopted.

The charge radius is computed from the charge density distribution as follows:

$$\langle r^2\rangle_{\rm ch} = \frac{1}{Z}\int d^3r\, r^2 \rho_{\rm ch}(\mathbf{r}) = \langle r^2\rangle_{\rm p} + r_{\rm p}^2 + \frac{N}{Z}(r_+^2 - r_-^2) + \delta\langle r^2\rangle_c, \tag{C9}$$

where

$$\langle r^2\rangle_{\rm p} = \frac{1}{Z}\int d^3r\, r^2 \rho_{\rm p}(\mathbf{r}), \tag{C10}$$

and the relativistic correction $\delta\langle r^2\rangle_c$ is

$$\delta\langle r^2\rangle_c = \frac{3\hbar^2}{4(Mc)^2} + \left(1 + \frac{1}{2\mu'_{\rm p}}\right)\frac{1}{Z}\int d^3r\, r^2\omega_{\rm p}(\mathbf{r}) + \frac{1}{Z}\int d^3r\, r^2\omega_{\rm n}(\mathbf{r}). \tag{C11}$$

Although not shown here, the integral of $r^2\omega_t(\mathbf{r})$ can be expressed as the expectation value of $\boldsymbol{\ell}\cdot\hat{\boldsymbol{\sigma}}$ ($\boldsymbol{\ell} = \mathbf{r}\times\mathbf{p}$).

[1] K. Heyde, *Basic Ideas and Concepts in Nuclear Physics*, 3rd ed. (Institute of Physics, Bristol, 2004).

[2] H. Nakada, Exposing minimal composition of Kohn-Sham theory and its extendability, Phys. Scr. **98**, 105007 (2023).

[3] I. Angeli and K. P. Marinova, Table of experimental nuclear ground state charge radii: An update, At. Data Nucl. Data Tables **99**, 69 (2013).

[4] P. Campbell, I. D. Moore, and M. R. Pearson, Laser spectroscopy for nuclear structure physics, Prog. Part. Nucl. Phys. **86**, 127 (2016).

[5] X. F. Yang, S. J. Wang, S. G. Wilkins, and R. F. Garcia Ruiz, Laser spectroscopy for the study of exotic nuclei, Prog. Part. Nucl. Phys. **129**, 104005 (2023).

[6] P. Aufmuth, K. Heilig, and A. Steudel, Changes in mean-square nuclear charge radii from optical isotope shifts, At. Data Nucl. Data Tables **37**, 455 (1987).

[7] T. Day Goodacre, A. V. Afanasjev, A. E. Barzakh, B. A. Marsh, S. Sels, P. Ring, H. Nakada, A. N. Andreyev, P. Van Duppen, N. A. Althubiti, B. Andel, D. Atanasov, J. Billowes, K. Blaum, T. E. Cocolios, J. G. Cubiss, G. J. Farooq-Smith, D. V. Fedorov, V. N. Fedosseev, K. T. Flanagan *et al.*, Laser spectroscopy of neutron-rich ^{207,208}Hg isotopes: Illuminating the kink and odd-even staggering in charge radii across the $N = 126$ shell closure, Phys. Rev. Lett. **126**, 032502 (2021).

[8] C. Gorges, L. V. Rodríguez, D. L. Balabanski, M. L. Bissell, K. Blaum, B. Cheal, R. F. Garcia Ruiz, G. Georgiev, W. Gins, H. Heylen, A. Kanellakopoulos, S. Kaufmann, M. Kowalska, V. Lagaki, S. Lechner, B. Maaß, S. Malbrunot-Ettenauer, W. Nazarewicz, R. Neugart, G. Neyens *et al.*, Laser spectroscopy of neutron-rich tin isotopes: A discontinuity in charge radii across the $N = 82$ shell closure, Phys. Rev. Lett. **122**, 192502 (2019).

[9] R. F. Garcia Ruiz, M. L. Bissell, K. Blaum, A. Ekström, N. Frömmgen, G. Hagen, M. Hammen, K. Hebeler, J. D. Holt, G. R. Jansen, M. Kowalska, K. Kreim, W. Nazarewicz, R. Neugart, G. Neyens, W. Nörtershäuser, T. Papenbrock, J. Papuga, A. Schwenk, J. Simonis *et al.*, Unexpectedly large charge radii of neutron-rich calcium isotopes, Nat. Phys. **12**, 594 (2016).

[10] F. Sommer, K. König, D. M. Rossi, N. Everett, D. Garand, R. P. de Groote, J. D. Holt, P. Imgram, A. Incorvati, C. Kalman, A. Klose, J. Lantis, Y. Liu, A. J. Miller, K. Minamisono, T. Miyagi, W. Nazarewicz, W. Nörtershäuser, S. V. Pineda, R. Powel *et al.*, Charge radii of ^{55,56}Ni reveal a surprisingly similar behavior at $N = 28$ in Ca and Ni isotopes, Phys. Rev. Lett. **129**, 132501 (2022).

[11] M. M. Sharma, G. Lalazissis, J. König, and P. Ring, Isospin dependence of the spin-orbit force and effective nuclear potentials, Phys. Rev. Lett. **74**, 3744 (1995).

[12] P.-G. Reinhard and H. Flocard, Nuclear effective forces and isotope shifts, Nucl. Phys. A **584**, 467 (1995).

[13] M. M. Sharma, G. A. Lalazissis, and P. Ring, Anomaly in the charge radii of Pb isotopes, Phys. Lett. B **317**, 9 (1993).

[14] H. Nakada and T. Inakura, Effects of three-nucleon spin-orbit interaction on isotope shifts of Pb nuclei, Phys. Rev. C **91**, 021302(R) (2015).

[15] H. Nakada, Further evidence for three-nucleon spin-orbit interaction in isotope shifts of nuclei with magic proton numbers, Phys. Rev. C **92**, 044307 (2015).

[16] H. Nakada, Properties of exotic nuclei and their linkage to the nucleonic interaction, Int. J. Mod. Phys. E **29**, 1930008 (2020).

[17] S. A. Fayans, Towards a universal nuclear density functional, JETP Lett. **68**, 169 (1998).

[18] S. A. Fayans, S. V. Tolokonnikov, E. L. Trykov, and D. Zawischa, Nuclear isotope shifts within the local energy-density functional approach, Nucl. Phys. A **676**, 49 (2000).

[19] P.-G. Reinhard and W. Nazarewicz, Toward a global description of nuclear charge radii: Exploring the Fayans energy density functional, Phys. Rev. C **95**, 064328 (2017).

[20] E. Caurier, K. Langanke, G. Martínez-Pinedo, F. Nowacki, and P. Vogel, Shell model description of isotope shifts in calcium, Phys. Lett. B **522**, 240 (2001).

[21] B. A. Brown and K. Minamisono, β^2 corrections to spherical energy-density functional calculations for root-mean-square charge radii, Phys. Rev. C **106**, L011304 (2022).

[22] A. J. Miller, K. Minamisono, A. Klose, D. Garand, C. Kujawa, J. D. Lantis, Y. Liu, B. Maaß, P. F. Mantica, W. Nazarewicz, W. Nörtershäuser, S. V. Pineda, P.-G. Reinhard, D. M. Rossi, F. Sommer, C. Sumithrarachchi, A. Teigelhöfer, and J. Watkins, Proton superfluidity and charge radii in proton-rich calcium isotopes, Nat. Phys. **15**, 432 (2019).

[23] H. Nakada, Irregularities in nuclear radii at magic numbers, Phys. Rev. C **100**, 044310 (2019).

[24] M. Bender, P.-H. Heenen, and P.-G. Reinhard, Self-consistent mean-field models for nuclear structure, Rev. Mod. Phys. **75**, 121 (2003).

[25] J. L. Friar and J. W. Negele, Theoretical and experimental determination of nuclear charge distributions, in *Advances in Nuclear Physics*, edited by M. Baranger and E. Vogt (Plenum, New York, 1975), Vol. 8, pp. 219–376.

[26] H. Kurasawa and T. Suzuki, The *n*th-order moment of the nuclear charge density and contribution from the neutrons, Prog. Theor. Exp. Phys. **2019**, 113D01 (2019).

[27] P.-G. Reinhard and W. Nazarewicz, Nuclear charge densities in spherical and deformed nuclei: Toward precise calculations of charge radii, Phys. Rev. C **103**, 054310 (2021).

[28] K. Bennaceur and J. Dobaczewski, Coordinate-space solution of the Skyrme-Hartree-Fock-Bogolyubov equations within spherical symmetry. The program HFBRAD (v1.00), Comput. Phys. Commun. **168**, 96 (2005).

[29] H. Nakada, Hartree–Fock–Bogolyubov calculations with Gaussian expansion method, Nucl. Phys. A **764**, 117 (2006).

[30] H. Nakada, Application of Gaussian expansion method to nuclear mean-field calculations with deformation, Nucl. Phys. A **808**, 47 (2008).

[31] J. Bartel, P. Quentin, M. Brack, C. Guet, and H.-B. Håkansson, Towards a better parametrisation of Skyrme-like effective forces: A critical study of the SkM force, Nucl. Phys. A **386**, 79 (1982).

[32] E. Chabanat, P. Bonche, P. Haensel, J. Meyer, and R. Schaeffer, A Skyrme parametrization from subnuclear to neutron star densities Part II. Nuclei far from stabilities, Nucl. Phys. A **635**, 231 (1998).

[33] M. Kortelainen, J. McDonnell, W. Nazarewicz, P.-G. Reinhard, J. Sarich, N. Schunck, M. V. Stoitsov, and S. M. Wild, Nuclear energy density optimization: Large deformations, Phys. Rev. C **85**, 024304 (2012).

[34] J. F. Berger, M. Girod, and D. Gogny, Time-dependent quantum collective dynamics applied to nuclear fission, Comput. Phys. Commun. **63**, 365 (1991).

[35] H. Nakada, Semi-realistic nucleon-nucleon interactions with improved neutron-matter properties, Phys. Rev. C **87**, 014336 (2013).

[36] H. Nakada and K. Sugiura, Predicting magic numbers of nuclei with semi-realistic nucleon–nucleon interactions, Prog. Theor. Exp. Phys. **2014**, 033D02 (2014).

[37] G. A. Lalazissis, S. Raman, and P. Ring, Ground-state properties of even–even nuclei in the relativistic mean-field theory, At. Data Nucl. Data Tables **71**, 1 (1999).

[38] G. Co', M. Anguiano, and A. M. Lallena, Charge radii of Ca isotopes and correlations, Phys. Rev. C **105**, 034320 (2022).

[39] H. De Vries, C. W. De Jager, and C. De Vries, Nuclear charge-density-distribution parameters from elastic electron scattering, At. Data Nucl. Data Tables **36**, 495 (1987).

[40] R. L. Workman *et al.* (Particle Data Group), Review of particle physics, Prog. Theor. Exp. Phys. **2022**, 083C01 (2022).

[41] H. Kurasawa, T. Suda, and T. Suzuki, The mean square radius of the neutron distribution and the skin thickness derived from electron scattering, Prog. Theor. Exp. Phys. **2021**, 013D02 (2021).